

ALMA Memo No. 541

Horizontal temperature variations at Chajnantor

Alison Stirling^{1,2} *, Angel Otárola^{3,4} †, Roberto Rivera³, J. Ruben Bravo⁵

1. Astrophysics Group, Cavendish Laboratory, Madingley Road, Cambridge, CB3 0HE UK

2. Met Office, FitzRoy Road, Exeter, EX1 3PB, UK

3. European Southern Observatory, Casilla 19001, Santiago 19, Chile

4. National Radio Astronomy Observatory, 949 North Cherry Avenue, 5th floor, Tucson, AZ 85721

5. ALMA OSF, San Pedro, Chile

February 24, 2006

1 Abstract

In August 2005 an observing campaign was conducted to measure the horizontal variability in the temperature profile above the Chajnantor site. The temperature profile is known to affect pointing and phase corrections, as well as amplitude calibrations, and so knowledge of the likely variation in temperature is essential for planning ancillary meteorological equipment for the site.

The campaign concentrated on analysing the atmosphere in two locations of the extended array configuration. In these two sites, radiosonde balloons were launched at regular intervals and high frequency surface measurements were taken using a meteorological mast. The results of the study have shown that the temperature profile in the first 100 m above the ground is strongly controlled by surface heating and cooling, and that variation in the altitude of the terrain can introduce horizontal temperature variations of up to 5 K over the site.

We have analysed the likely impact of these temperature variations on pointing and phase corrections, looking at the errors introduced by assuming that the temperature profile from one location can be used to estimate the pointing and phase corrections at the second location. We find that pointing errors introduced by using a temperature profile from a different part of the Chajnantor site are of order 0.3'' at an elevation of 60 degrees. Path errors introduced as a result of using the distant temperature profile are of order 2%. These errors are similar in magnitude if an idealised temperature profile is used, in which a constant lapse rate is assumed, in conjunction with the measured surface temperature at that location.

In addition we have measured the parameters required for future atmospheric modelling studies of the site, for example the net radiation (incoming minus outgoing, shortwave and longwave) in August peaks at 460-495 W m⁻² at midday, and the surface albedo is 0.6. The surface sensible

*Email: alison.stirling@metoffice.gov.uk

†Email: aotarola@email.arizona.edu

and latent heat fluxes peak at $\sim 300 \text{ W m}^{-2}$ and 40 W m^{-2} respectively, and the roughness length is measured to be $\sim 1 \text{ cm}$. In the presence of antennas, this is expected to increase to 10 cm in the extended configuration, and 160 cm in the compact configuration, increasing the mechanically induced turbulence at the site.

2 Introduction

The vertical temperature profile affects both the refractive index and brightness temperature of the atmosphere. Knowledge of the refractive index is important in determining the antenna pointing corrections required, and fluctuations in this quantity introduce phase errors to the visibility measurements. It is envisaged that water vapour radiometry will correct for the wet component of phase, but knowledge of the conversion factor between path and brightness temperature is itself determined by knowledge of the temperature profile – with 0.2-0.7% error being introduced into the phase determination for every Kelvin error in temperature of the fluctuating water vapour layer (for PWV < 0.7 mm, Stirling *et al.*, 2004; memo 496).

While horizontal variations in temperature tend to be quickly equalised in the troposphere, heating and cooling from the ground influence the lowest 100 m significantly. If there is significant slope in the terrain, then the surface heating affects air at different pressure levels depending on the height of the terrain. In this case horizontal gradients in the temperature profile are introduced, and air flows from the hot region to the cooler region to equalise the temperature. The surface wind pattern is therefore likely to be strongly influenced by the local terrain. The relative timescales of surface heating to air flow determine the amplitude of the horizontal temperature variation.

The layout of this report is as follows: we outline the observational set up for the campaign in Section 3 and present the surface observations from the met mast in Section 4 including surface energy fluxes, temperature and humidity data, and wind data from which a roughness length for the terrain is deduced (the method for this is given in an appendix to this report). In Section 5 we present the radiosonde data, showing how the temperature and humidity evolves during the day, and how it differs between the two sites. Section 6 looks at the impacts of horizontal temperature variations on pointing correction estimation and w.v.r. phase correction. For each we calculate the error in the corrections in the case where the two temperature profiles are swapped over – of relevance if a single temperature profile is to be measured and used for all corrections at the site, and in the case where a simple idealised profile is combined with actual surface measurements. The conclusions are given in Section 7.

3 The campaign observations

We chose two locations that will form part of ALMA’s extended array configuration. The first site was close to the array centre, near the NRAO and ESO containers on the Chajnantor plateau. This is at an altitude of $\sim 5000 \text{ m}$, and we will refer to it as site ‘A’. The second site was located 7 km almost due west of site A, and is located between two of the originally proposed¹ antenna pad sites

¹The position of these antenna pads in the Y+ confi guration has subsequently been changed owing to potential loss of natural habitat for a population of viscachas, however the drop in altitude across the new confi guration is $\sim 300 \text{ m}$, which is similar to the difference in altitude between our two test sites. (Holdaway, private communication).

in the outer regions of the Y+ configuration (see Otárola & Holdaway, 2002). This was at the base of Cerro Negro at an altitude of 4650 m, and we will refer to this second location as site ‘B’. The locations are marked on the map in Fig. 1.

Measurements were taken both from a meteorological mast (loaned to us by the University of Reading in the UK), and from radiosonde ascents, with the mast providing continuous surface readings, and the sondes providing intermittent soundings of the vertical temperature and humidity profiles.

The mast supported the following instruments, with the associated measurements shown in brackets:

- ◇ pulse output cup anemometer (Vector instruments, A101ML) (wind speed)
- ◇ potentiometric wind vane (Vector instruments, A100) (wind direction)
- ◇ temperature and humidity sensor (Vaisala)
- ◇ solarimeter (Kipp and Zonen, CM5) (solar flux)
- ◇ net radiometer (Kipp and Zonen, NR Lite) (incoming short-wave minus outgoing long-wave radiation)
- ◇ flux plate (Rimco, HP3) (temperature gradient at ground surface).

Data was collected every five seconds, and stored in averages of five minute intervals. The mast was erected at the Chajnantor site for five days, and then moved down to the Cerro Negro site for a further two days.

Radiosondes were launched over four days at the two sites, including an intensive 24 hour period in which a sonde was launched every 90 minutes at alternating Chajnantor and Cerro Negro locations. Figure 2 shows the location and times of all the sondes launched. For this campaign, we have used AIR-5A radiosondes, which transmitted readings of temperature, humidity and pressure at a sample rate of 1 Hz. The wind speed and direction were retrieved from the radiotheodolite measurement of the Doppler shift in the 1600 MHz carrier signal, combined with the change in angular position on the sky. The helium balloons for the sondes were filled to a diameter of ~ 1.5 m, aiming for an ascent rate of 5 ms^{-1} . The sondes were tracked up to an altitude of 7000 m. This relatively low maximum height was designed to allow sufficient time to move the equipment down to the lower site, while sampling the whole of the boundary layer, where the effects of the ground have their greatest impact. Before each sonde was launched, ground checks of radiosonde readings were performed, measuring temperature with a hand-held thermometer, humidity with a psychrometer, and pressure using a G.P.S. barometer. When the sondes were launched from the Chajnantor site (A), the met-mast data was also available for comparison.

4 Results from the Reading Met Mast

4.1 Solar fluxes and surface energy balance

Heat is transferred to the atmosphere from the ground in two ways – via conduction of the heat to air molecules at the surface (known as sensible heating), or via evaporation of ground-based water which is then released into the air (known as latent heating). The amount of heat available is given by:

$$R_{N0} - G_0 = H_0 + \lambda E_0, \quad (1)$$

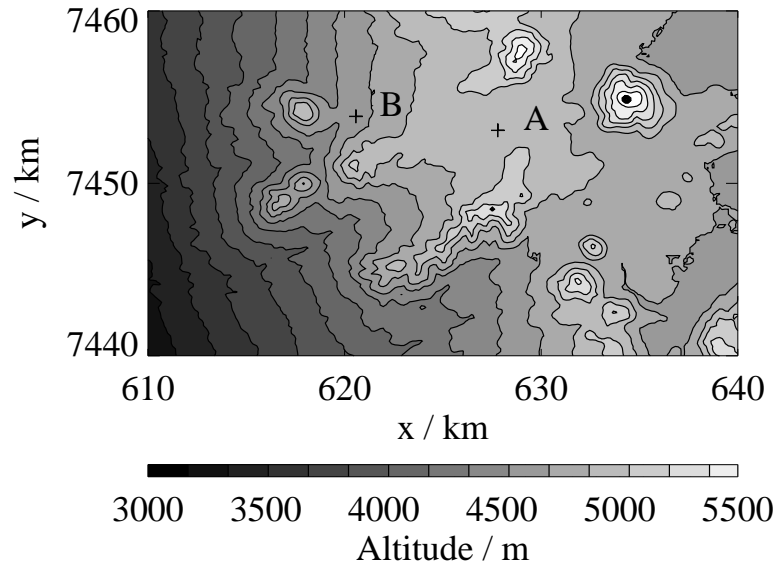


Figure 1: Map of the Chajnantor region showing the two sites (marked with crosses) where the observations were taken. Site A is at an altitude of 5000 m near the NRAO and ESO containers, and site B is at an altitude of 4650 m, at the base of Cerro Negro.

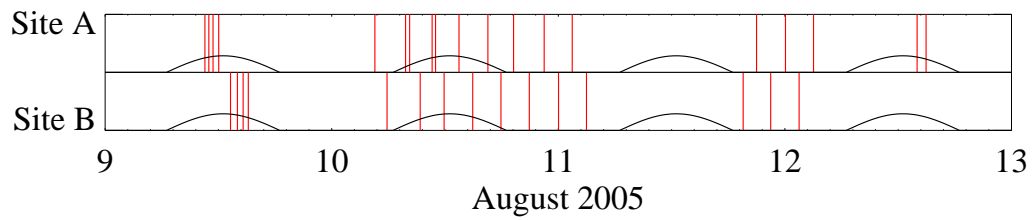


Figure 2: Summary of the times of radiosonde launches at the two sites during August 2005. Each vertical line indicates a different launch. Days are represented in local time, with the sinusoidal curve representing the height of the sun in the sky.

where R_{N0} is the net incoming (solar) radiation minus the outgoing (longwave) radiation, G_0 is the heat flux into the ground, H_0 is the sensible heat flux, and λE_0 is the latent heat flux (with $\lambda = 2.5 \times 10^6 \text{ J kg}^{-1}$ being the specific heat of vaporisation).

We can also calculate the albedo for the terrain by taking the ratio of the reflected long-wave radiation to the incoming short-wave radiation, *i.e.*

$$A = 1 - \frac{R_N}{S_g}. \quad (2)$$

Figure 3 shows the radiation and ground heat components of the fluxes, from which the total surface heating can be calculated. The solar fluxes peak at 1004 W m^{-2} at Site A, and 1027 W m^{-2} at Site B, while the net radiation, R_N peaks at 495 W m^{-2} at Site A, and 460 W m^{-2} at Site B. The albedo is measured to be 0.6 at both sites during the day, and is consistent with the predictions of Baumer (1990) of the albedo of soil containing no vegetation.

Our next interest is to quantify the partition of the surface fluxes into sensible and latent heat. There are number of methods for calculating this, and here we adopt one of the simpler approaches by making use of the radiosonde data. The ratio of sensible to latent heat fluxes from the ground (known as the Bowen ratio, B) is related directly to the surface gradients in temperature and water vapour:

$$\frac{H_0}{\lambda E_0} = B = \frac{c_p \overline{(w'\theta')}_0}{\lambda \overline{(w'q')}_0} = \frac{c_p \partial\theta/\partial z}{\lambda \partial q/\partial z}, \quad (3)$$

where $\overline{w'\theta'}$ is the potential temperature flux at the surface, $\overline{w'q'}$ is the water vapour flux, and subscript 0 denotes the surface value. c_p is the specific heat of air at constant pressure, $\partial\theta/\partial z$ is the gradient in potential temperature at the surface, and $\partial q/\partial z$ is the gradient in water vapour density at the surface. By calculating this ratio from the radiosonde ascents, we can obtain an estimate for the relative contributions from the sensible and latent heat fluxes:

$$H_0 = (R_{N0} - G_0) B / (1 + B); \quad \lambda E_0 = (R_{N0} - G_0) / (1 + B). \quad (4)$$

Here we make the simplistic approximation that the Bowen ratio remains constant throughout the day, taking the view that modifications to this will have only a small impact on our estimates. From the radiosonde launches, we measure an average Bowen ratio of $B \simeq 7$. Figure 4 shows the calculated sensible and latent heat fluxes. The sensible heat peaks at around 300 W m^{-2} at mid-day, and drops to $\sim -30 \text{ W m}^{-2}$ at night, while the latent heat flux peaks at $\sim 40 \text{ W m}^{-2}$ at mid-day, and decreases to $\sim -5 \text{ W m}^{-2}$ at night. The latent heat flux can be converted into units of the rate of increase of PWV, with the peak value of $\sim 40 \text{ W m}^{-2}$ corresponding to an increase in the PWV of 0.06 mm per hour. The release of water vapour from the ground during the day has also been observed in FTS measurements over the site at dawn (Scott Paine, private communication). It should be noted that this result will vary throughout the year, depending on the soil moisture content, and that the PWV amount at the site is likely to be predominantly affected by winds advecting dry air over the plateau from the west.

4.2 Temperature and water vapour amount

Figures 5 and 6 show the evolution of temperature and water vapour at the two different sites. While the temperature displays a strong diurnal evolution, the water vapour evolution appears to

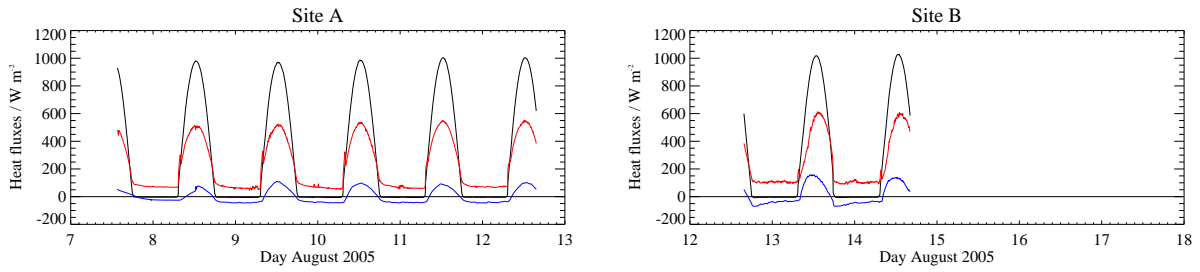


Figure 3: Time series of incoming solar (black), outgoing longwave (red, sign inverted) and upwards ground heat (blue) fluxes for site A and site B.

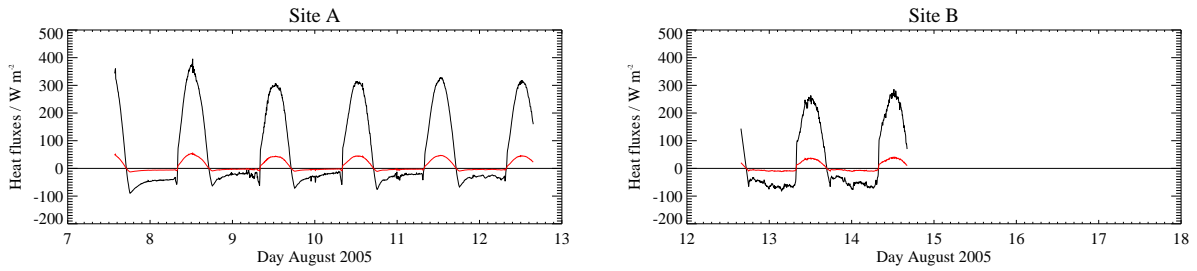


Figure 4: Time series of latent (red) and sensible heat (black) fluxes for site A and site B.

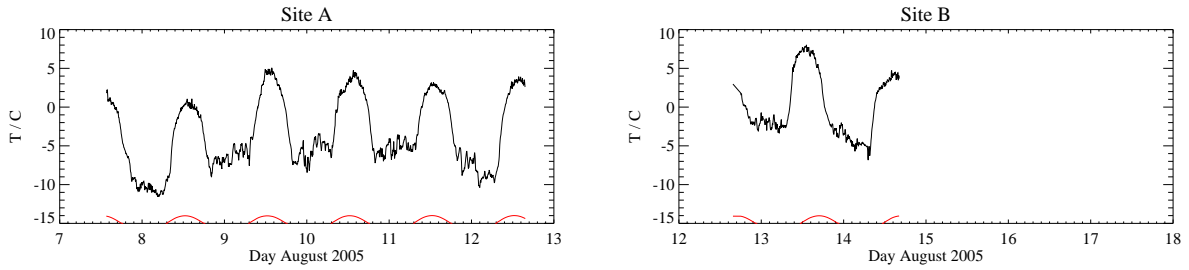


Figure 5: Time series of temperature at site A (left) and site B (right).

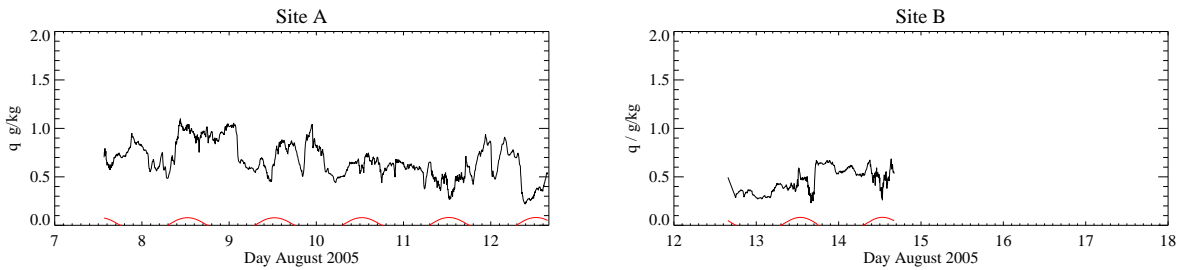


Figure 6: Time series of water vapour amount at site A (left) and site B (right).

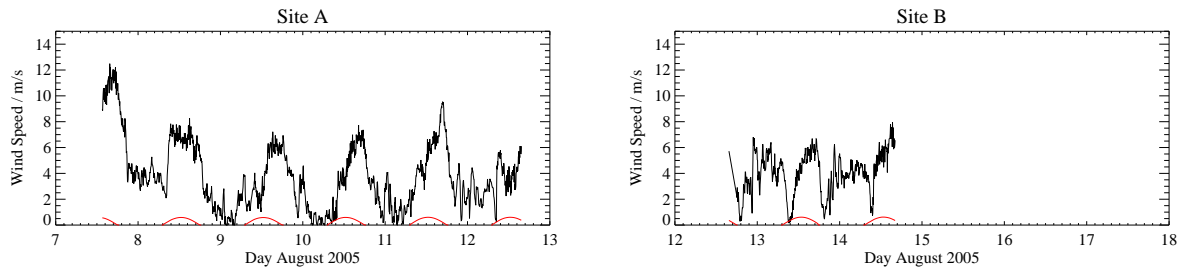


Figure 7: Time series of wind speed at site A (left), and site B (right).

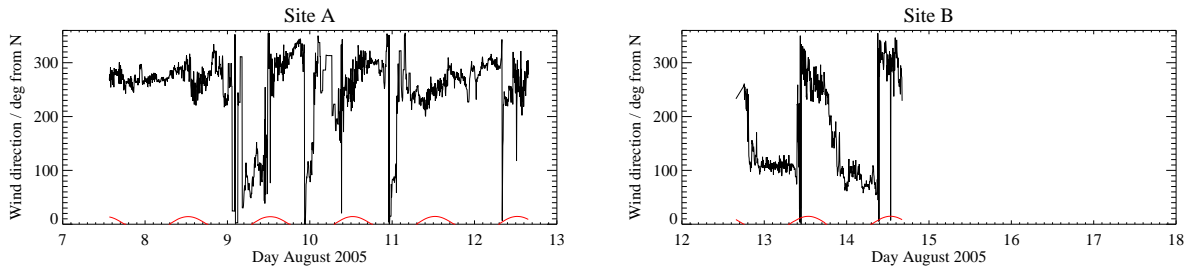


Figure 8: Time series of wind direction at site A (left), and site B (right). Angle is measured clockwise round from due North. So 90 degrees is due East, 180 is due South, and 270 due West.

be considerably more erratic, suggesting that the amount of water vapour present in the atmosphere is significantly larger than the amount injected into the atmosphere via the surface heat fluxes.

4.3 Wind and direction

Figures 7 and 8 show the wind speed and direction at the site. At Chajnantor (site A), there is a clear diurnal pattern to the wind speeds, falling to near zero at night. At site B, while the wind speeds do not display such a marked variation, the wind direction shows a strong diurnal pattern, coming from the west during the daytime, and the east at night. The diurnal behaviour is in both cases likely to be caused by cold air draining downhill. At Chajnantor, which apart from isolated peaks is the highest point in the terrain, the air drains downhill and outwards from Chajnantor, creating a divergent air flow, giving rise to calm conditions at the surface. Meanwhile site B lies on terrain with a strong east-west gradient, and the downhill flow of air (also known as katabatic winds) dominates at night, giving rise to a wind flow from the east. The particularly pronounced diurnal signal of these winds during the observation period suggests that during this time, the winds and temperature profiles were dominated by the local effects of the terrain.

4.4 Roughness length

Close to the surface, the wind is affected by frictional drag from the ground. Quantification of this frictional effect is important for the modelling of the atmosphere, as it affects the amount of shear generated at the surface, and thereby the amount of mechanically induced turbulence – which is the main source of phase fluctuations during the night.

The frictional effect of the surface gives a characteristic form to the wind profile, which is depen-

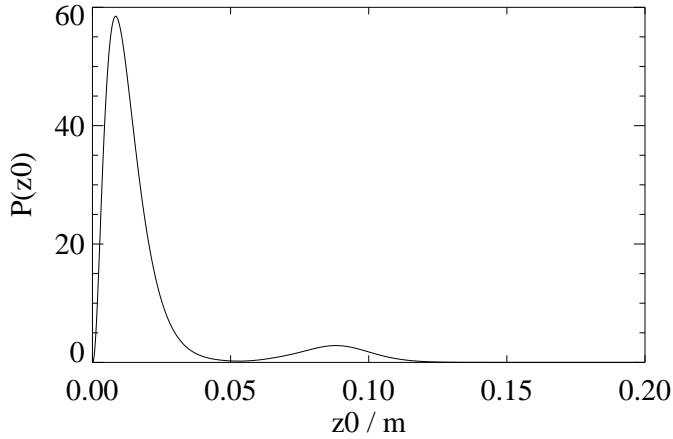


Figure 9: Estimate of the roughness length at Chajnantor (without antennas).

dent only on the wind stress and the roughness length. While the wind stress is a function of wind speed, the roughness length remains constant, so by measuring the shape of this profile for a range of wind speeds the roughness length can be inferred. To do this we have used wind data from the Reading met mast, and the ESO anemometer, which provide data at heights 3 and 4 m above the ground respectively, and estimated a probability distribution for the roughness length.² A description of the theory and method used to calculate the roughness length is given in Appendix 11.

The probability distribution is shown in Fig. 9, which gives an estimate for the roughness length of $z_0 = 0.8 \pm 0.7$ cm. The small sub-peak in probability around $z_0 = 0.1$ m has its main contribution from winds from a ENE direction. This is in the path of the containers, which may have disrupted the flow.

Of course, the roughness length at the site will change in the presence of antennas, with two parameters affecting the value. The first, λ_1 , is the cross-sectional area of the antenna normal to the wind multiplied by the number of antennas per unit area. The second, h_c is the height of the antenna. An approximate relation for z_0 in the range of interest is given by:

$$z_0 = \alpha \lambda_1 h_c \quad (5)$$

(Lettau 1969), where $\alpha \sim 0.5$. So for an antenna height, h_c , of 15 m, and width, w of 12 m, the roughness length is expected to scale as:

$$z_0 = \alpha h_c^2 w N_{\text{ant}} / D^2 \simeq 0.1 / D \text{ (km)}^2, \quad (6)$$

where D is the horizontal length scale of the array. This gives roughness lengths of $z_0 = 0.1, 1.6$ m for a 1 km, and 250 m square array of 64 antennas respectively.

²While there are two other anemometers at this site, they are positioned just above the containers, and so estimates of the roughness length are likely to be affected by the flow around the containers.

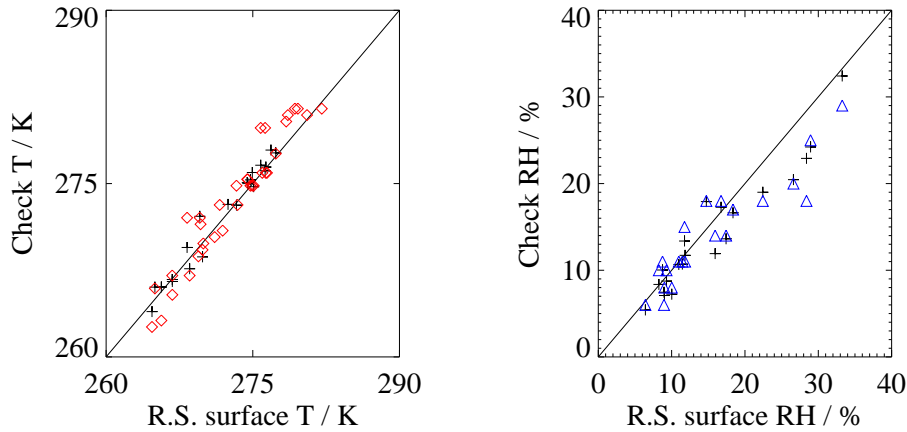


Figure 10: Figure showing comparisons of the radiosonde surface (R.S.) measurements of temperature (left) and relative humidity (right) with the Reading met mast (crosses), a hand-held thermometer (diamonds), and the ESO weather station (triangles).

5 Results from the radiosonde launches

The aim of the radiosonde launches was to compare the temperature profiles at two different points of the ALMA extended array configuration, with a view to quantifying the likely impact of horizontal temperature variation on pointing corrections and water vapour radiometer corrections.

Since the sondes used were several years old, it was important to check that they were taking reasonable measurements before being released. To do this, we took temperature and humidity measurements with a hand-held psychrometer, and have used met mast data from Chajnantor to check the temperature and humidity readings. The hand-held psychrometer readings turned out to give erroneous results – probably because the dew point temperature was frequently below 0 C, and the wet cloth froze before an accurate reading could be obtained. Figure 10 shows how the radiosonde data at the surface compares with independent measurements of temperature and humidity. The temperature measurements of the sondes launched agree to within ~ 1 K with the other instruments at the site, while the humidity measurements from the ESO and Reading met masts lie within ~ 3 % for humidities below 20%. There is some indication that there may be a bias of the radiosonde receivers towards more humid results above 20% humidity, however, since the main goals of this work are to understand the nature of the temperature profiles, we will not explore this effect further here.

It is also important to consider the trajectory of the sondes, in particular, given the nature of this study, the altitude of terrain they pass over. Figure 11 shows the terrain over which the balloons passed and the distance from the ground directly below them as they climb in altitude. It shows that while the balloons do indeed drift over land of different altitudes, the change in altitude of the terrain only starts deviating significantly from the launch site altitude when the balloons have risen over 1 km, by which height there is only limited influence from the ground.

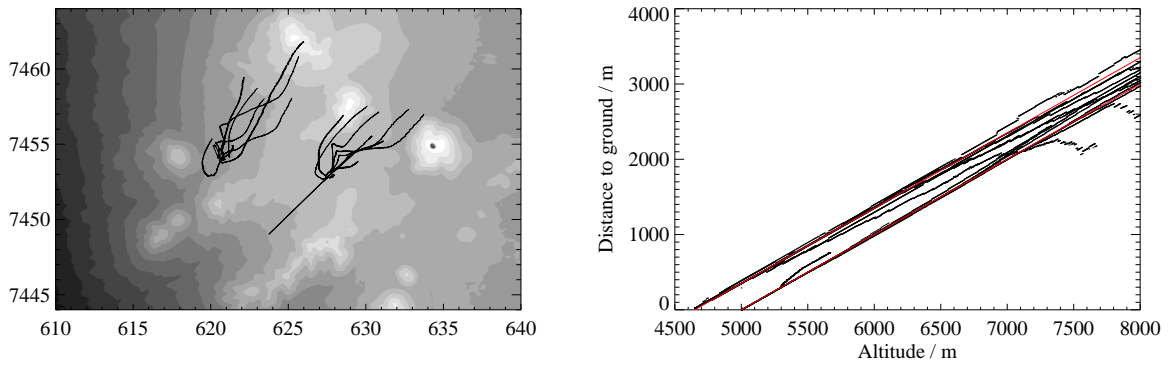


Figure 11: Left panel shows the horizontal trajectories of the balloons from the two launch sites A and B. Right panel shows how the distance of the balloon from the ground directly below it changes with altitude as the balloon ascends. Red lines indicate the distance to the ground if the balloon had a vertical ascent profile.

5.1 Temperature and water vapour profiles

In this section we present the radiosonde profiles measured at the two sites. We will first consider the general structure and evolution of the profiles, before going on to consider how the profiles differ at the two sites.

5.1.1 Daytime

Figures 12 and 13 show the potential temperature and moisture profiles from sondes launched during the day. The temperature profiles have a characteristic form, with a steep decrease in temperature with height in the first 100 m, as heat is imparted to the atmosphere via surface conduction. Then in a layer 100-1000 m from the ground, the potential temperature remains near constant, as convective turbulent eddies mix the layer. Capping this mixed layer is a strong temperature inversion, which spans a layer varying between 100 and 500 m in thickness. Above this layer, the atmosphere is free from the effects of the surface, and follows a near constant lapse rate of -7 K km^{-1} (corresponding to a potential temperature gradient of $\sim +3 \text{ K km}^{-1}$).

The top left panel of Fig. 12 shows a clear example of the growth of the convective layer before noon – as the temperature increases, the convective energy increases, and turbulent eddies start to erode the temperature inversion, thereby increasing the thickness of the layer. After mid-day, the temperature of the mixed layer falls rapidly. This is caused in part by radiative-cooling, but mainly because of an orographically-induced wind circulation that is set up to equalise the temperature of the plateau with the ambient, off-plateau surroundings. As the mixed layer cools, the inversion at the top of the layer is strengthened, thus decreasing the impact of convective erosion on layer height.

The water vapour profiles show a steep gradient close to the surface, created by the evaporation of ground water. Between 100-1000 m from the ground the profile gradients become much smaller, reflecting the turbulent mixing as a result of the convective activity. In the mixed layer, however, the gradients are still larger than in the potential temperature profiles, and suggests that a large contribution to the water vapour profiles is from horizontal advection of moist air from the prevailing winds.

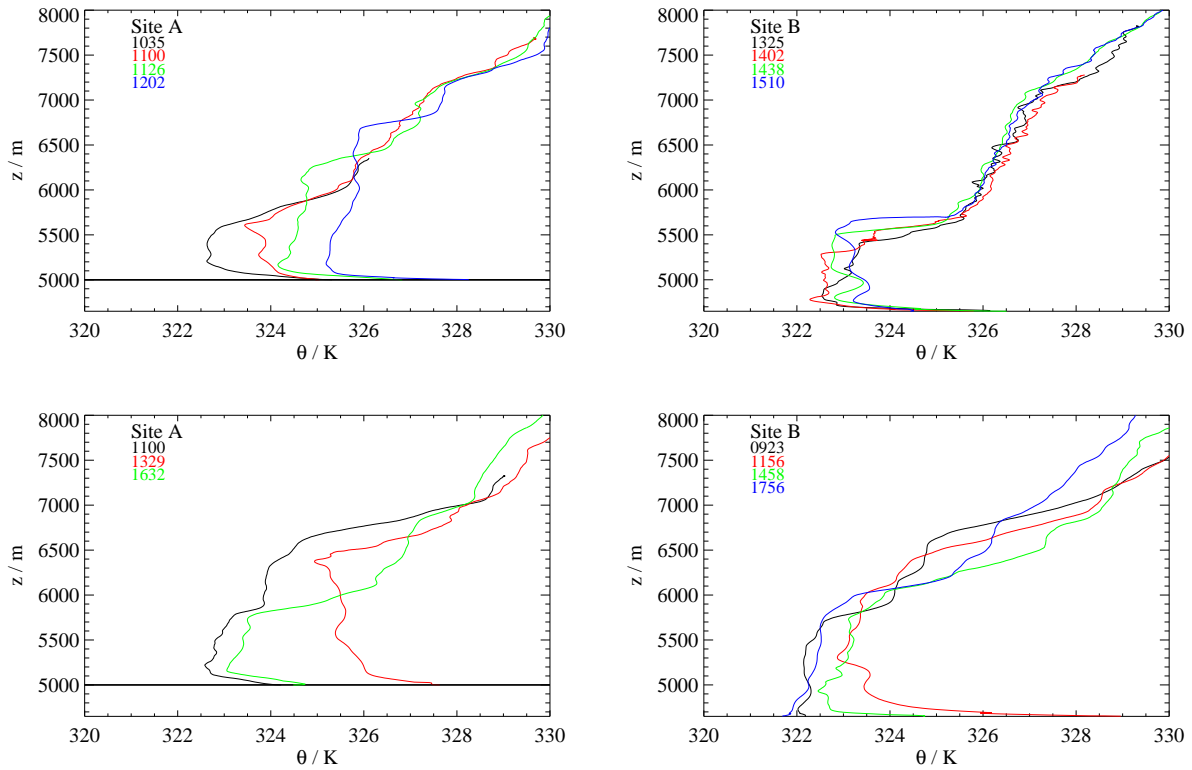


Figure 12: The daytime potential temperature profiles taken from sondes launched from site A (left column), and site B (right column). Each panel contains launches from a single day, and the local times of launches are marked in the top left of each panel. (Potential temperature is a measure of temperature which removes the effect of adiabatic cooling as a result of the decrease in air pressure with height, see *e.g.* memo 517 for more details.) The line colour gives the order of the launches, with black being the first launch during that day, followed by red, green and then blue.

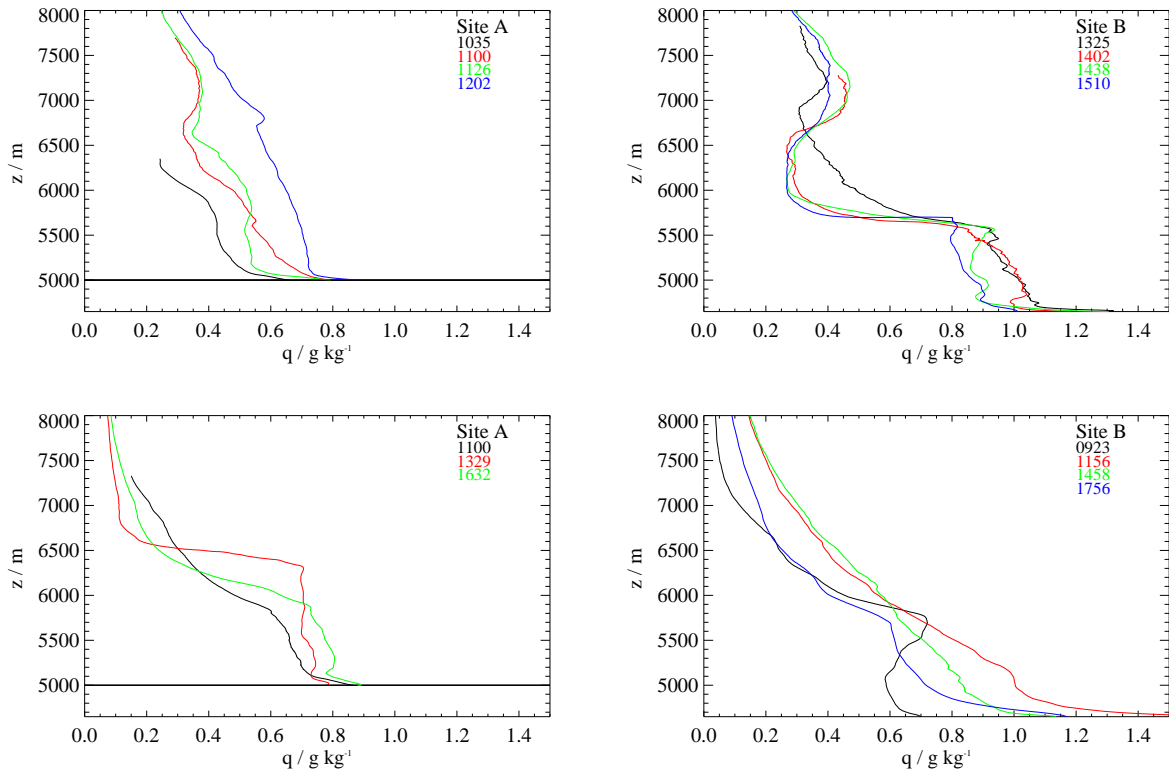


Figure 13: Figure showing how the daytime moisture profiles evolve at site A (left column), and site B (right column). The line colours denote the same times as in figure 12.

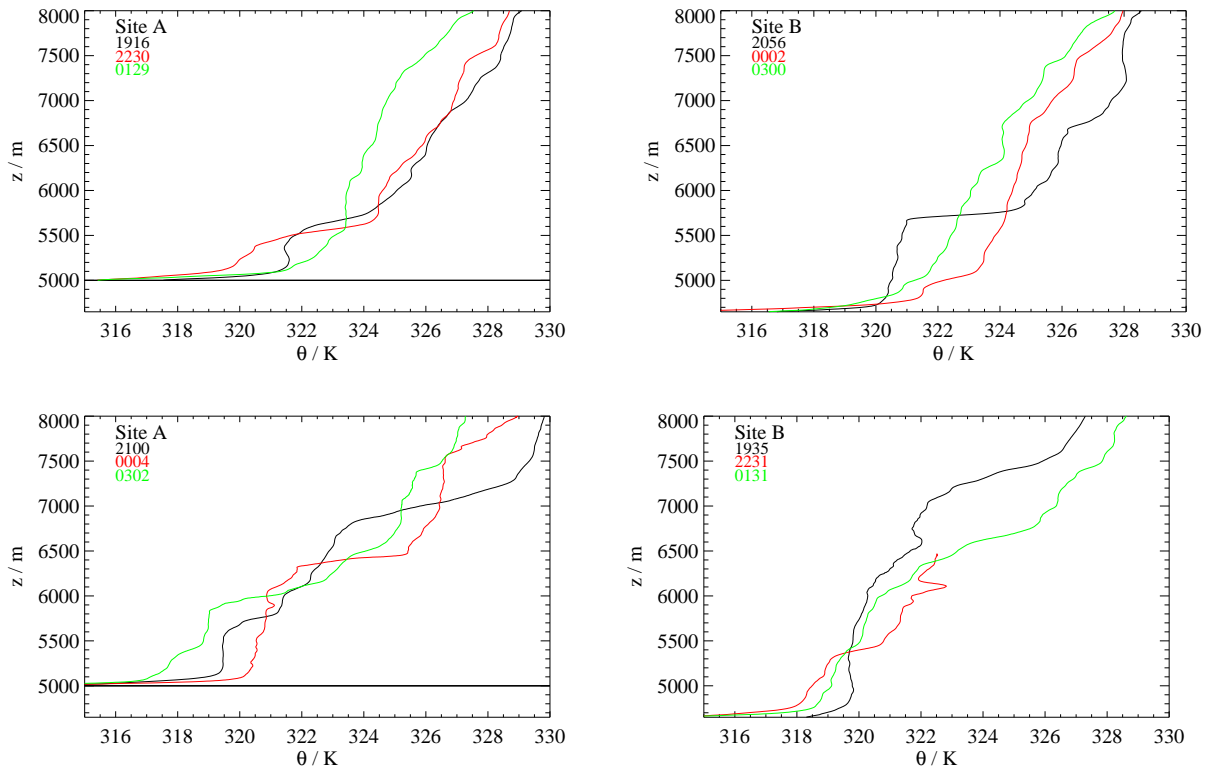


Figure 14: Figure showing how the night time potential temperature profiles evolve at site A (left column), and site B (right column). The colour key in each plot gives the local times of the profiles plotted.

5.1.2 Night-time

Now we consider the night time structure and evolution of the temperature and moisture profiles. Figures 14 and 15 show the temperature and moisture profiles at each of the sites as they evolve during the night.

The potential temperature profiles now increase strongly with height in the lowest 100 m, with temperature lapse rates of $\sim -4 \text{ K km}^{-1}$. Above this layer follows a relatively neutral layer, containing the remnants of the day's convective layer (this is known as the residual layer). This is capped with a second inversion at a height of $\sim 1000 \text{ m}$ above the ground, above which the temperature profile is independent of the ground, and has a lapse rate of $\sim -7 \text{ K km}^{-1}$.

The evolution of the profile at night appears to be somewhat complex, with the residual layer warming after sunset before eventually cooling. The warming is in part because as the residual layer thickness decreases, the capping temperature inversion is lowered, bringing warmer air lower down. This sinking of air is likely to be a stronger effect up at the Chajnantor plateau, where katabatic draining winds create low-level divergence, giving rise to subsidence. At the lower site, B, the warming may be in part due to long-wave radiation from the surrounding mountain faces.

5.1.3 Comparisons between site A and site B

In this section we compare the temperature profiles between the two sites. Since the sondes could not be launched simultaneously, an interpolation of the profiles is required to compare the tem-

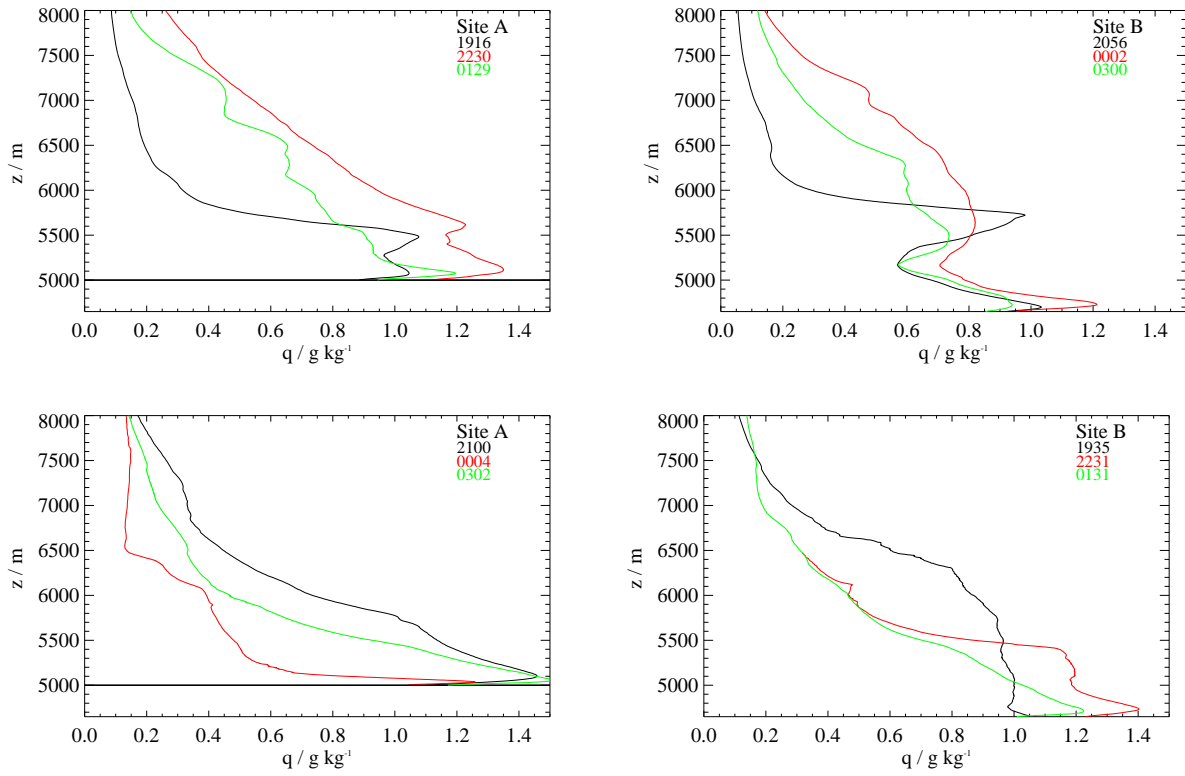


Figure 15: Figure showing how the night time moisture profiles evolve at site A (left column), and site B (right column). The launch times shown are the same as in figure 14.

perature profiles at a given time. We concentrate on the intensive observations during a 24 hour period for this comparison, where sondes were released every 90 minutes at alternating sites (*i.e.* every three hours at each site, giving eight profiles per site). Figure 16 shows a time series of the temperature profiles, with linear interpolation performed between consecutive launches, and wrapping between the last and first sondes to give a full 24 hour period. The bars at the top of the figure show the timings of the sonde launches. The greatest variation in temperature is at the surface, with a diurnal variation of ~ 14 K at both sites. This variation falls sharply to ~ 6 K in the layer 200–500 m from the ground, and to ~ 4 K 500 m and higher above the ground.

Figure 17 shows the temperature differences between the two sites during this period. We consider these in two ways – firstly comparing the temperature at the same height above sea level, and secondly comparing the temperature at the same height above the ground (since the ground is at different altitudes, these measures are not the same). Above 6000 m above sea level, the temperature difference is relatively small throughout the 24 hour period, with differences of < 1 K. Between 5500 m and 6000 m, the higher site is 2-3 K warmer, while at night, this difference drops to < 1 K. Between 5000 m and 5500 m, site A is 5 K warmer, during the day, and 5 K cooler at night. Comparing temperatures at the same height above the ground shows temperature differences of around 2-3 K for heights up to 2000 m above the site, with site A tending to be systematically warmer above 500 m.

In view of the plan for a single temperature profiler at the site, one might ask how best to estimate the temperature profile at other locations of the array, particularly where the altitude of the terrain differs from that at the temperature profiler. The results from our study suggest that in the lowest 500 m, a good estimate would be to assume the temperature profile is the same as that deduced from the profiler, but with the heights taken relative to the ground, while above 500 m the heights should be taken above sea level. Some interpolation around 500 m may be needed to smooth out artificial jumps in such a profile.

In the next section we look at the impacts of using an estimate for the temperature profile on pointing and phase corrections. Here we adopt an even simpler estimate, and try using the entire temperature profile as measured relative to the ground from one site as the estimate for temperature at the other site.

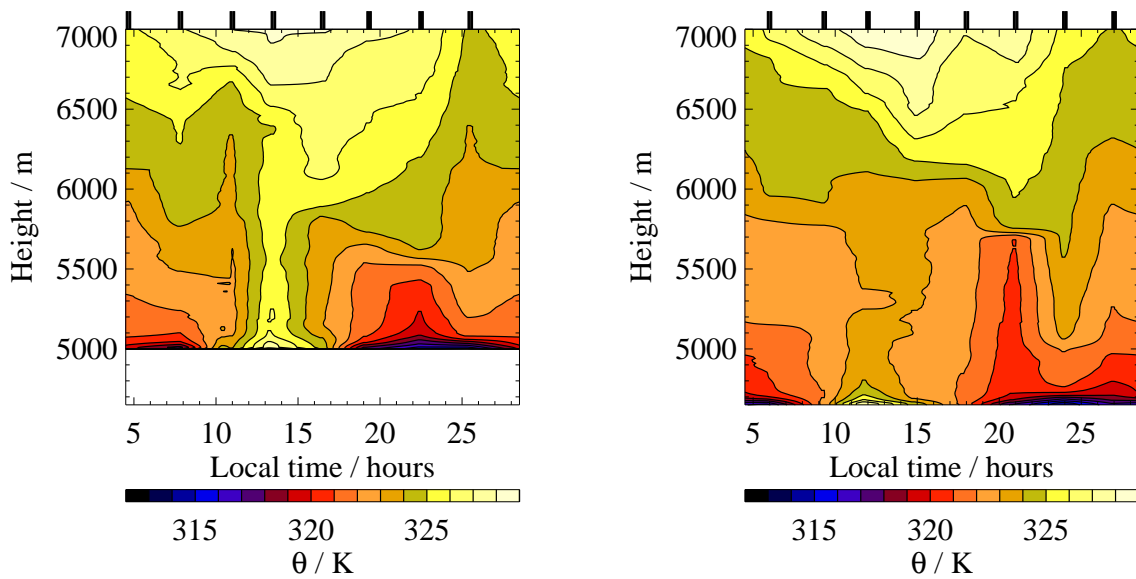


Figure 16: Time series of potential temperature with height at site A (left) and site B (right). Bars at the top indicate the times of the radiosonde launches.

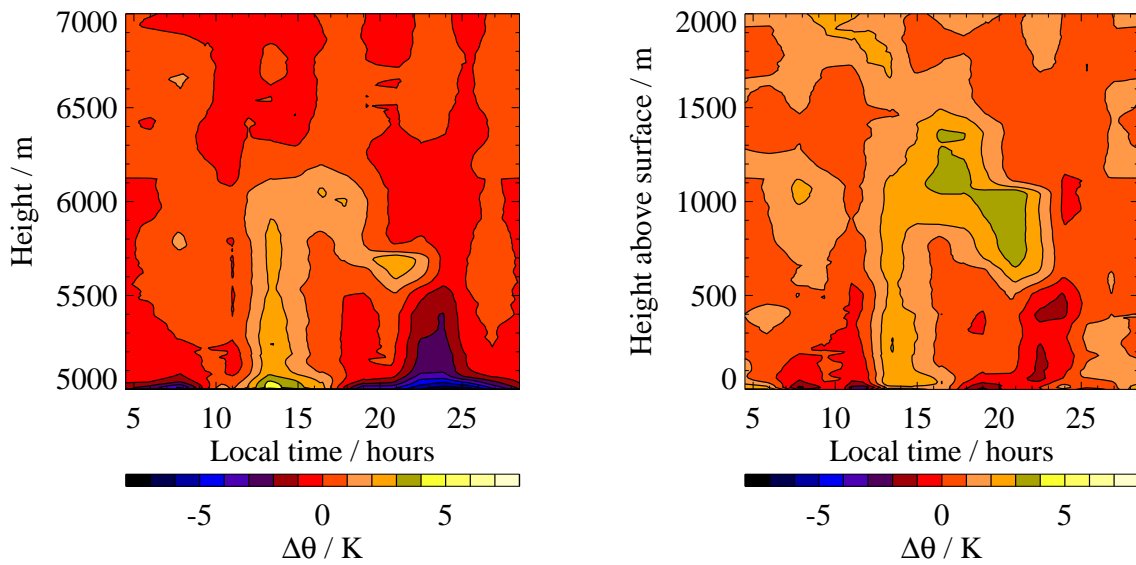


Figure 17: Difference between temperature at the two sites (temperature at site A minus that of site B). Left panel shows how the temperature differs for a given pressure level between the two sites. Right panel shows how the temperature differs for a given height above the surface.

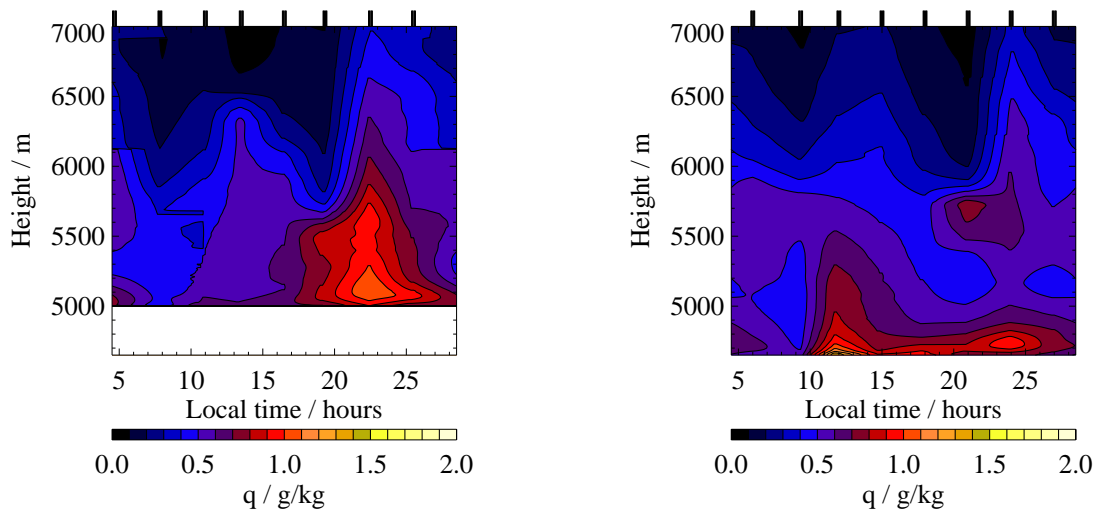


Figure 18: Time series of water vapour density with height at site A (left) and site B (right). Bars at the top indicate the times of the radiosonde launches.

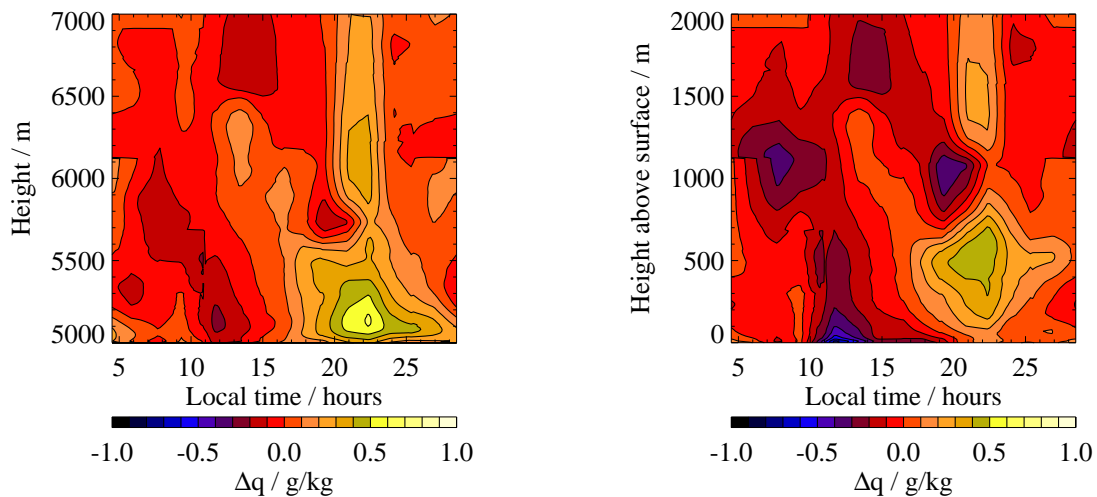


Figure 19: Difference between water vapour at the two sites (site A - site B). Left panel shows how the water vapour differs for a given pressure level between the two sites. Right panel shows how the water vapour differs for a given height above the surface.

6 Impact of temperature on pointing and phase correction

6.1 Pointing correction

In this section we consider the impact of horizontal temperature variability at the site on pointing corrections. The angular deviation required to observe a source in the presence of the atmosphere compared is given by (e.g. Mangum 2001; memo 366 and references therein):

$$\Delta z = r_0 n_0 \sin z_0 \int_1^{n_0} \frac{dn}{n (r^2 n^2 - r_0^2 n_0^2 \sin^2 z_0)^{1/2}} \quad (7)$$

where Δz is the angular deviation in radians, r_0 is the radius of the earth, n_0 is the refractive index at the surface, z_0 is the angle from zenith of the observed source, n is the refractive index at a given height in the atmosphere, and r is the radius of the earth plus the given height in the atmosphere.

The refractive index can be calculated from the Smith-Weintraub equation, which we use in the following form:

$$10^6(1 + n) = \frac{\alpha R \rho}{\mathcal{M}_d} + \left[\frac{\beta}{\mathcal{M}_v} - \frac{\alpha}{\mathcal{M}_d} \right] R q \rho + \frac{\gamma R q \rho}{\mathcal{M}_v T} \quad (8)$$

where $R = 8.314 \text{ J mol}^{-1} \text{ K}^{-1}$ is the universal gas constant, $\mathcal{M}_d = 28.96 \text{ g mol}^{-1}$ is the molecular weight of dry air in the troposphere, and $\mathcal{M}_v = 18.02 \text{ g mol}^{-1}$ is the equivalent for water vapour. ρ is the air density, T is the temperature in Kelvins, q is the mass fraction of water vapour (units kg kg^{-1}), and α , β , and γ are constants given by: $\alpha = 77.6 \times 10^{-2} \text{ K Pa}^{-1}$, $\beta = 64.8 \times 10^{-2} \text{ K Pa}^{-1}$, $\gamma = 3.776 \times 10^3 \text{ K}^2 \text{ Pa}^{-1}$ (see *e.g.* Stirling *et al.*, 2005; memo 517 for a derivation).

We have considered three scenarios to explore the impact of temperature:

1. In the first, the temperature profiles taken from the intensive 24 hour observing period (Fig. 16) are interpolated to provide estimates of the temperature profile at each hour of the day, and at each site. These are then used to estimate the pointing correction required by the atmosphere up to a height of 7000 m (where our observations stop).
2. In the second, we construct idealised temperature profiles that use the observed surface temperature, and a constant lapse rate of -6.8 K km^{-1} (this is an average value found for earlier radiosonde campaign launches, as quoted in memo 496.)
3. In the third, we swap the temperature profiles for the two different sites around, so that the profile above site A becomes the profile above site B and vice versa. (For simplicity we have treated these temperature profiles as having heights relative to the ground surface, so in effect the temperature profile from site A is lowered to lie above site B, and that from site B is raised to sit above site A). The use of a temperature profile from a single location as the profile for all other locations is a possible strategy if there is a single temperature sounder at the site.

For each of these scenarios, we have calculated the pointing correction that would be obtained. Clearly, using the actual temperature profiles provides the ‘true’ pointing correction (for this region of the atmosphere), while the second and third scenarios will provide an estimate for the pointing correction. In all of these cases we have set the relative humidity to zero, in order to isolate the impact of the temperature profile.

Figure 20 shows how the pointing estimates change with time of day and with different elevations. The difference between the ‘true’ pointing correction, and the estimated ones (from scenarios

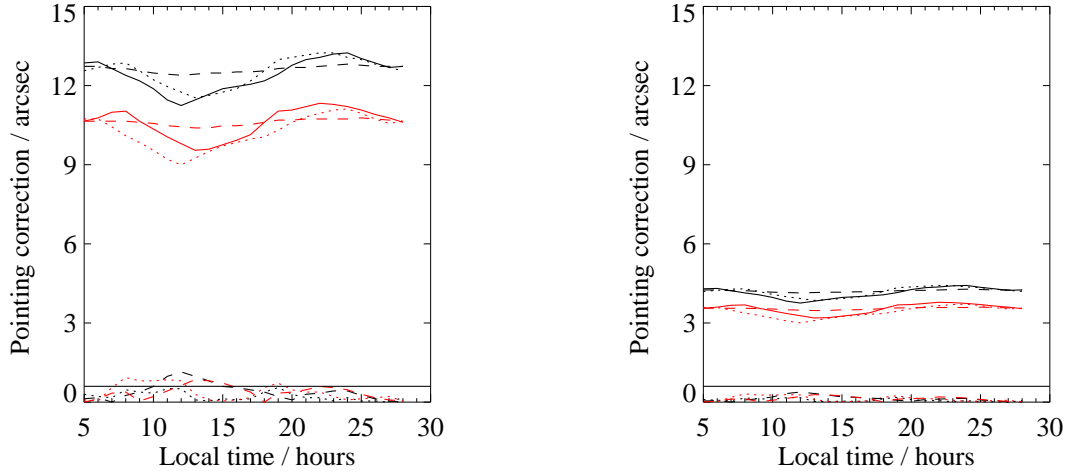


Figure 20: Plot showing how the pointing correction changes at the two sites. Left panel is for an elevation of 30 degrees, right panel for an elevation of 60 degrees. Red lines are for site A, black lines for site B. Solid lines show the pointing correction required using the temperature profile measured from the radiosondes (this is in some sense the ‘true’ pointing correction). Upper dashed lines show the pointing correction if only the measured surface temperature is used, and the profile is approximated by a constant lapse rate of -6.8 K km^{-1} . Upper dotted lines show what the pointing correction would be if the temperature profiles at sites A and B were swapped, as explained in Section 6.1. The straight solid line shows ALMA’s target of 0.6” pointing accuracy. Lower dashed lines show the (absolute) difference between the ‘true’ pointing correction, and that used if an assumed constant lapse rate is used. Lower dotted lines show the (absolute) difference between the true pointing correction and that obtained by swapping the temperature profiles around.

two and three) are also plotted. The results show that at elevations above 60 degrees, any of these strategies would produce a pointing accuracy below the ALMA goal of 0.6 arc secs. At lower elevations, however, the use of the measured surface temperature with a constant lapse rate throughout the 24 hour period gives rise to significant differences in pointing correction during the night when the true lapse rate deviates significantly from the -6.8 K km^{-1} assumed. The use of the temperature profile from one site at the other site gives errors lower than 0.6 arc secs, suggesting that the use of a single temperature profile as measured from a sounder may be adequate for the pointing requirements.

6.2 Phase correction

We now consider the impact of the temperature profile on estimates of the wet phase component using water vapour radiometry. The change in path length due to water vapour variations (ΔL) is obtained from:

$$\Delta L = \sum_i \frac{w_i \Delta T_i^{\text{BRI}}}{dT/dL_i}, \quad (9)$$

where ΔT_i^{BRI} is the change in brightness temperature in channel i , dT/dL_i is the sensitivity parameter for channel i , and w_i is a weight to allow the radiometer channels to be weighted differently. (See Stirling *et al.*, 2004; memo 496 for more details). The sensitivity parameter dT/dL_i is a function both of the water vapour amount and atmospheric parameters such as the distribution of

water vapour, the height of the fluctuating layer, and the temperature profile.

In this analysis, we have used idealised water vapour profiles and a variety of temperature profiles to calculate the sensitivity parameter for each radiometer channel at each site. The temperature profiles used are as in subsection 6.1 (radiosonde profiles interpolated onto an hourly grid; constant lapse rate of -6.8 K km^{-1} up to 15 km with measured surface temperature; temperature profile at site A used at site B and vice versa). The PWV has been scaled to be 1 mm, and we have used weights of:

$$w_1 = 0.18; \quad w_2 = 0.48; \quad w_3 = 0.29; \quad w_4 = 0.048 \quad (10)$$

as in memo 496 (bottom half of table 5, half way between PWV=0.7 and PWV=1.3).

In each case the sensitivity parameter is measured by making a 1% change to the entire water vapour profile, and taking the ratio of the change in brightness temperature to the change in path length. By allowing the whole water vapour profile to change, the temperature at every level is of importance in determining dT/dL , and so this measure of dT/dL can be considered to be maximally sensitive to the temperature profile, and so the errors retrieved can be considered as a worst-case scenario in which fluctuations in water vapour occur throughout the atmosphere.

We have measured the sensitivity parameter for the above three temperature profiles, and estimated the fractional path length error to be:

$$\frac{\epsilon(\Delta L)}{\Delta L} = \sum_i w_i \frac{\Delta dT/dL_i}{dT/dL_i} \quad (11)$$

where $\Delta dT/dL_i = dT/dL_i$ (guessed T profile) $- dT/dL_i$ (actual T profile). Figure 21 shows that using the temperature profile from site A at site B and vice versa introduces a path length error of between 1-2%. Use of a constant lapse rate of -6.8 K km^{-1} and the measured surface temperature also introduces an error of between 1-2%.

While these errors fall within the requirements for w.v.r., when combined with uncertainties in the heights of fluctuating PWV layers, and the shape of the water vapour profile, there may be a case for improving on this temperature estimate by using the profile as measured relative to the ground below 500 m, and the profile as measured relative to sea level above 500 m, with some simple interpolation in between (see figure 22 for a schematic representation).

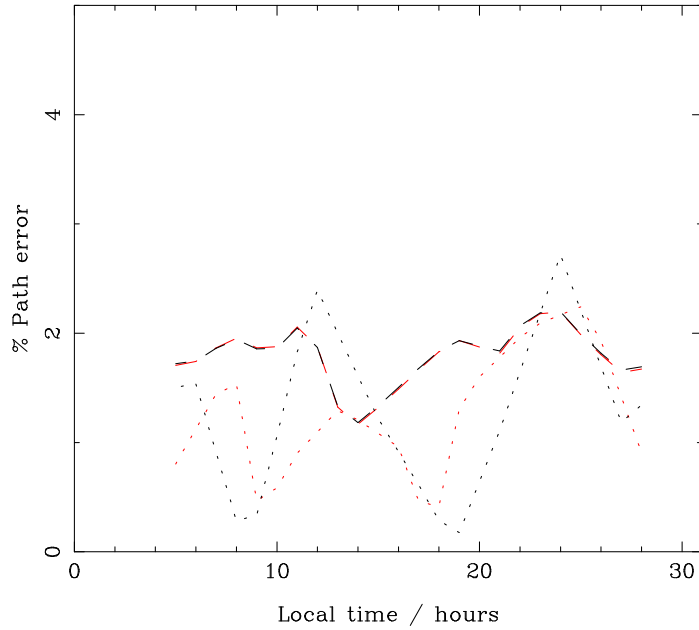


Figure 21: Fractional path error due to errors in the estimation of the temperature profile. Red lines are for site A, black for site B. Dashed lines show the error in the estimated path if the temperature profile from site A is used at site B and vice versa (see text). Dotted lines show the error if an assumed lapse rate of -6.8 K km^{-1} is used along with the measured surface temperature.

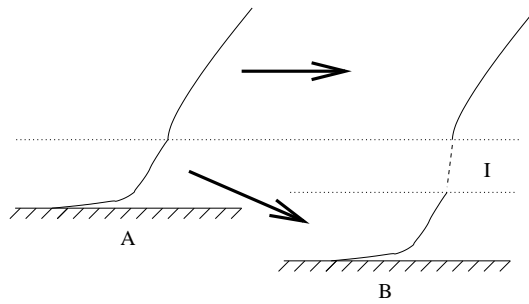


Figure 22: Schematic representation of a possible approach to estimating the temperature profile above locations at different altitudes. While the profile in the lower part of the atmosphere is lowered on to the new site, the upper part of the profile is transferred across with no change in height. I indicates the region in which a simple interpolation would be required.

7 Conclusions

In this report we have presented the results of a meteorological observing campaign at Chajnantor which was designed to measure the horizontal variations in temperature, and their likely impact on pointing and phase corrections. We also measured the surface heat fluxes and roughness length at the site, with a view to allowing realistic atmospheric simulations of the plateau.

The temperature in the lowest 100 m above the ground is found to be strongly controlled by the surface heat fluxes, and where the altitude of the terrain varies significantly, this can introduce horizontal temperature variations of up to 5 K.

In view of the plan to have a single temperature profiler at the site, we have investigated the errors introduced into pointing and phase corrections by using the profile at one location as an estimate for the profile at the second location. This introduces errors of around 0.3" at an elevation of 60 degrees, which is within ALMA's specification for pointing accuracy. A similar analysis for w.v.r. phase correction, which is also dependent on the temperature profile, shows that a single temperature profile used over the entire site can introduce errors of 1-2% in the retrieved path. A simple idealised model for the temperature profile in which the surface temperature is combined with a constant lapse rate representative of the average lapse rate above 500 m yields similar errors. In both cases these errors could be reduced further by approximating the temperature profile above each antenna to be the same as that from the profiler as measured relative to the ground in the lowest 500 m, where the effects of the surface dominate over large-scale atmospheric conditions, and above 500 m using the heights taken relative to sea level, since in this region, the temperature shows little horizontal variation for a given pressure level.

We note that, while not considered here, the temperature variability data obtained during this campaign could also be of use in evaluating the accuracy of amplitude calibration calculations.

We have measured solar fluxes, outgoing radiation and ground heat fluxes at the site, enabling us to deduce that the albedo is around 0.6, and that the surface sensible and latent heat fluxes peak around 300 W m^{-2} and 40 W m^{-2} respectively. We have used wind data from two met masts to calculate the roughness length, which is found to be 1 cm, although it is expected to increase in the presence of antennas, with a value around 10 cm when the array is in the extended configuration, and up to 160 cm when in the compact configuration. The presence of the antennas will increase the contribution of mechanically generated turbulence generated at the site, with a larger impact coming from the more compact configurations.

8 References

- Baumer, O.W. 1990 'Prediction of soil hydraulic parameters.' In: WEPP Data Files for Indiana. SCS National Soil Survey Laboratory, Lincoln, NE.
- Garratt, J.R., 1982, 'The atmospheric boundary layer' Cambridge Atmospheric and Space Science Series
- Lettau, H., 1969, 'Note on aerodynamic roughness-parameter estimation on the basis of roughness-element description' J.Appl. Meteor, **8**, 828-832
- Mangum, J., 2001, ALMA memo 366, 'A telescope pointing algorithm for ALMA'
- Otárola, A., Holdaway M.A., 2002, ALMA memo 419, 'The Y+ Long-Baseline Configuration To



Figure 23: Preliminary tests of the radiosonde system. Left to right: Ruben (behind balloon), Roberto, Angel, and Jorge.

Achieve High Resolution With ALMA'

Stirling, A.J., Hills, R.E., Richer, J.S., Pardo, J.R., 2004, ALMA memo 496 'Estimation of phase errors under varying atmospheric conditions'

Stirling, A.J., Holdaway, M., Hills, R.E., Richer, J.S., 2005, ALMA memo 515, 'Calculation of integration times for WVR'

Stirling, A.J., Richer, J.S., Hills, R.E., Lock, A.P., 2005, ALMA memo 517, 'Turbulence simulations of dry and wet phase fluctuations at Chajnantor: Part I: The Daytime Convective Boundary Layer'

9 Dedication

We dedicate this report to Roberto Rivera, who was killed in a car accident very shortly after this field campaign. He was instrumental in the preparation and execution of this work, and his dedication, sense of humour and enthusiasm kept us going in the long nights listening to radiosonde signals. The remaining authors are greatly saddened by loss of this colleague and friend.

10 Acknowledgements

The authors would like to thank Giles Harrison and Andrew Lomas at the University of Reading for the loan of the met mast, Charlotte Hermant at the JAO and Suitay Chang at the OSF for organising its transport in Chile, and Joel Brand at the Cavendish Laboratory for assisting with the transport from the UK.

We would also like to thank Vincente Ruiz and Jorge Riquelme for their assistance during the radiosonde launch campaign, Robb Randall for the loan of a psychrometer, and Mark Holdaway and Richard Hills for useful comments on this report.

11 Appendix

Roughness length derivation

In this section the relationship between roughness length and wind speed will be described briefly, and we present a method for estimating and our estimate of the roughness length from anemometer data taken from two masts at different heights at the Chajnantor site (site A).

In the surface layer, the wind profile u , has a log dependence on height, z :

$$u = \frac{u_{*0}}{k} \log(z/z_0) + \Phi(z) \quad (12)$$

(*e.g.* Garratt, 1982, sec 3.3.2) where k is the von Karman constant, a dimensionless parameter, widely measured to be 0.4. $u_{*0} = \langle u'w' \rangle_0$ is the surface friction velocity, and z_0 is the roughness length. Φ is an additional function, derived from Monin-Obukhov similarity theory, that is required if the potential temperature profile deviates from neutral conditions (*i.e.* there is a vertical gradient in potential temperature). While the surface friction velocity depends on the wind speed, the roughness length, z_0 , is a constant intrinsic to the surface, (although it can be a function of wind direction).

Since, Φ depends on stability, we first define a stability parameter, L , known as the Obukhov length, which is defined as:

$$L = \frac{-u_{*0}^3 \theta}{kg \langle w'\theta' \rangle_0}, \quad (13)$$

where θ is the potential temperature at the surface, and $\langle w'\theta' \rangle_0$ is the heat flux from the ground (*i.e.* $H_0/\rho/c_p$ from equation 1). A physical interpretation of this length is that it is proportional to the height above the surface at which the buoyant production of turbulence dominates over the mechanical production. When $\langle w'\theta' \rangle_0 > 0$, *i.e.* the ground imparts heat to the atmosphere, L is negative, and in this regime, turbulence is dominated by the buoyant convective motion of the air. When $\langle w'\theta' \rangle_0 < 0$, the larger the value of L , the thicker the layer close to the ground in which mechanical shear drives the turbulence.

For $0 \leq z/L < 1$, *i.e.* stable conditions such as those found at night, Φ is a simple, linear function of height:

$$\Phi(z) = \beta z/L \quad (14)$$

where $\beta \simeq 4.7$.

In the range $-5 < z/L < 0$ *i.e.* mildly unstable conditions during the daytime, the adjustment parameter is given by:

$$\xi = (1 - \gamma z/L)^{1/4} \quad (15)$$

$$\Phi(z) = 2 \log[(1 + \xi)/2] + \log[(1 + \xi^2)/2] - 2 \tan^{-1}(\xi) + \pi/2 \quad (16)$$

where $\gamma \simeq 16$.

We have used wind data from the Reading met mast (u_1) at site A and the ESO anemometer (u_2) to fit for both u_{*0} and z_0 . The wind data has been averaged into hourly bins, and for each hour, we have generated two statistics: u_1/u_2 , which is sensitive mainly to the roughness length, and $u_1 - u_2$, which is sensitive mainly to u_{*0} . We then create a grid of u_{*0} and z_0 values, and calculated the theoretical equivalent statistics for that particular time period, based on equations 12, 14 and 16 (using surface flux data to determine L .) For each value of u_{*0} and z_0 , we calculate the difference between the measured and theoretical statistics via a χ^2 value *i.e.* :

$$\chi^2(u_1, u_2 | u_{*0}, z_0) = \frac{\left[f(u_1^{\text{act}}, u_2^{\text{act}}) - f(u_1^{\text{model}}, u_2^{\text{model}}) \right]^2}{\sigma_f^2} + \frac{\left[g(u_1^{\text{act}}, u_2^{\text{act}}) - g(u_1^{\text{model}}, u_2^{\text{model}}) \right]^2}{\sigma_g^2}, \quad (17)$$

where $f(u_1, u_2) = u_1/u_2$, and $g(u_1, u_2) = u_1 - u_2$, and the errors, σ_f , and σ_g are estimated using the variance in wind speed from the Reading met mast data (which is binned into 5 minute intervals).

Assuming Gaussian statistics, we can turn this into a probability distribution:

$$p(u_{*0}, z_0) \propto \exp[-\chi^2]. \quad (18)$$

We can then obtain a probability distribution that is independent of u_{*0} by integrating over u_{*0} :

$$p(z_0 | u_1^i, u_2^i) \propto \int p(u_{*0}, z_0) du_{*0}, \quad (19)$$

and we can then combine the estimates from each hour of wind data, by multiplying the individual probability distributions for z_0 together:

$$p(z_0) \propto \prod_i p(z_0 | u_1^i, u_2^i). \quad (20)$$

The results of this analysis are shown in figure 9 in subsection 4.4.